# Spaceborne assessment of the Soviet Union's role in the 1990s methane slowdown

Tai-Long He[1*] (taihe@uw.edu)
Ryan J. Boyd[1,a] (rb0319@princeton.edu)
Daniel J. Varon[2] (danielvaron@g.harvard.edu)
Alexander J. Turner[1*] (turneraj@uw.edu)

[1]Department of Atmospheric Sciences, University of Washington, Seattle, 98195, WA, USA
[2]John A. Paulson School of Engineering and Applied Sciences, Harvard University, Cambridge, 02138, MA, USA
[a]now at Department of Civil and Environmental Engineering, Princeton University, Princeton, 08544, NJ, USA

**Corresponding authors:** Tai-Long He and Alexander J. Turner

---



---

# Spaceborne assessment of the Soviet Union's role in the 1990s methane slowdown

Tai-Long He[1], Ryan J. Boyd[1,a], Daniel J. Varon[2], and Alexander J. Turner[1]

[1]Department of Atmospheric Sciences, University of Washington, Seattle, 98195, WA, USA
[2]John A. Paulson School of Engineering and Applied Sciences, Harvard University, Cambridge, 02138, MA, USA
[a]now at Department of Civil and Environmental Engineering, Princeton University, Princeton, 08544, NJ, USA

**Methane is the second most important anthropogenic greenhouse gas, amounting to 60% of the radiative forcing from $CO_2$ since pre-industrial times based on emitted compound. Global atmospheric methane concentrations rose by 10-15 ppb/yr in the 1980s before abruptly slowing to 2-8 ppb/yr in the early 1990s. This period in the 1990s is known as the "methane slowdown" and has been attributed to the collapse of the former Soviet Union (USSR) in 1991, which may have decreased the methane emissions from oil and gas operations. Here we develop a methane plume detection system based on probabilistic deep learning and human-labelled training data. We use this method to detect methane plumes from Landsat 5 satellite observations over Turkmenistan from 1986 to 2011. We find an increase in both the frequency of methane plume detections and the magnitude of methane emissions following the collapse of the USSR in 1991. We estimate a national leak rate from oil and gas infrastructure in Turkmenistan of more than 10% at times, which suggests the socioeconomic turmoil led to a lack of oversight and widespread infrastructure failure in the oil and gas sector. Our results contradict the theory that the 1990s methane slowdown was driven by the collapse of the USSR, which we find led to an increase in methane emissions.**

## Introduction

Atmospheric methane has exhibited both periods of rapid growth and stabilization since in situ observations began in the early 1980s. There has been much debate about the causes of these variations[1, 2, 3, 4, 5, 6, 7, 8, 9, 10, 11, 12, 13, 14, 15, 16]. One such variation occurred in the early 1990s when the methane growth rate ($d[\mathrm{CH}_4]/dt$) abruptly declined from 10-15 ppb/yr to 2-8 ppb/yr in 1992. This change in the methane growth rate is referred to as the "methane slowdown". Previous work observed a decline in the inter-polar difference (IPD; difference between Arctic and Antarctic methane concentrations) that coincided with the methane slowdown[1, 2]. Analysis of stable carbon isotopes of methane ($\delta^{13}$C-$CH_4$) suggested a decline in isotopically heavy sources[4] in the early 1990s, such as oil and gas (O&G). Following this, previous work[1, 2, 4] hypothesized that the collapse of the USSR caused the methane slowdown due to a decrease in O&G production, resulting in lower methane emissions from a high-latitude source. This hypothesis is compatible with both the constraints from the IPD and $\delta^{13}$C-$CH_4$. However, recent work has shown how the IPD is affected by extra-polar emissions and variations in atmospheric transport[17], meaning the IPD may not reflect changes in high-latitude sources as originally hypothesized. Regarding $\delta^{13}$C-$CH_4$, there is large overlap in the isotopic source signatures[6] and, as such, they do not unambiguously constrain fossil fuel sources. Uncertainties in historical methane emissions from wetlands and the methane sink further complicate the interpretation. Here we assess the role of the collapse of the USSR on the methane slowdown in 1992.

Analysis of economic data shows a decline in gas production from former USSR republics following the collapse[18]. This economic data can be used to construct a "bottom-up" estimate of methane emissions. Fig. S1 shows the O&G production data and a bottom-up estimate of methane emissions for the USSR and Turkmenistan[19]. Bottom-up methods predict a decline in methane emissions from USSR O&G of 1400 Gg/yr between 1992 and 1997. Turkmenistan's O&G emissions are predicted to decline by 700 Gg/yr. The severe decline in Turkmen gas production was driven by the decrease and eventual complete cessation of demand from republics in the former USSR, primarily Ukraine, between 1993 and 1998[20]. Bottom-up methods attribute half of the decline in USSR O&G methane emissions to Turkmenistan, suggesting that it was a particularly important contributor to the methane slowdown in 1992. As such, quantifying historical changes in O&G methane emissions in Turkmenistan is crucial for understanding the drivers of the methane slowdown.

Recent work from Varon *et al.*[21] demonstrated how land surface imaging satellites can be used to detect and quantify methane emissions from large point sources. Briefly, these satellites have bands in the shortwave infrared (SWIR) that cover methane absorption features near 1.6 $\mu$m and 2.2 $\mu$m. The high spatial resolution of these land surface imaging satellites (20–30 m) results in a high signal-to-noise ratio in the vicinity of large methane point sources. This has been used in a number of recent studies[21, 22, 23] to quantify methane emissions from O&G operations over the past few years using Landsat 8-9 and Sentinel-2A/B. Landsat 4-5 were the first in the Landsat series to include SWIR bands, potentially allowing the quantification of historical methane plumes. Landsat 5 launched in March 1, 1984 and operated until June 5, 2013. The historical records from Landsat 4-5 may provide new insights into the drivers of variations in atmospheric composition over the past half century.

Here we develop a methane plume detection system based on an ensemble of deep learning models and trained using human-labelled methane plume masks. This plume detection system is then applied to the 26-year record from Landsat 5 over Turkmenistan. We quantify the point source methane emissions from O&G operations in Turkmenistan before and after the collapse of the USSR. Through comparison with economic data, we estimate a national leak rate from O&G operations in Turkmenistan.

# Detection of Methane Sources in Turkmenistan

The 1986–2011 Landsat 5 operational period provides data both before and after the collapse of the USSR. Methane plumes were detected over Turkmenistan using the ensemble deep-learning model (see Methods) and emissions ($Q$) were quantified using the integrated methane enhancement (IME) method[24, 25, 21]. Fig. 1 shows two examples of methane plumes detected in Turkmenistan. Plume detections are based, in part, on the normalized difference in top-of-atmosphere reflectance in the two SWIR bands ($dR$), similar to other normalized difference indices used in land surface imaging work. We then use a radiative transfer model[25, 21] to determine the methane column anomalies needed to reproduce the observed $dR$. Figs. 1a and 1d show the $dR$; Figs. 1c and 1f show the associated methane column anomalies. The ensemble deep-learning method allows us to calculate regions of high and low confidence in the detected plumes, indicated by the contours in Figs. 1b and 1e. We define our high (low) confidence region as pixels that are classified as a methane plume by more than 75% (10%) of the deep learning ensemble models. Methane emissions for the plumes are then computed using the IME method with the methane anomalies from Landsat 5, plume masks from the plume detection method, and renanalysis windspeed data from the ECMWF Reanalysis v5[26]. Application of this method to automatically detect plumes and quantify emissions with noisy data from the older series of Landsat instruments (4-5) required a number of developments (see Methods). To our knowledge, the methane plume shown in the top row of Fig. 1, from 1986, is the oldest methane plume ever observed from space.

Fig. 1g shows the location of all detected plumes from Landsat 5. In total, we detected 776 plumes between 1986 and 2011. Each plume was manually examined after detection to evaluate the robustness of the methodology and minimize false detections. Three prominent clusters of plumes can be seen in the southeast, northeast, and in the west along the Caspian Sea. These regions all have extensive O&G operations. Many of these regions have been noted by previous work using instruments on modern satellites: Sentinel-5P[27], Sentinel-2A/B[28, 23], and Landsat 8[28]. We observe intermittent plumes along pipelines in the central and eastern O&G fields in Turkmenistan. To our knowledge, these are some of the first methane plume detections in these regions. Fig. 1h shows the statistics of all the detected plumes. The distribution of methane emissions is lognormally distributed with a mean (median) emission rate of 10.4 t/hr (6.1 t/hr). A lognormal distribution of methane emissions is consistent with previous work characterizing the distribution of methane emissions from O&G operations[24, 29, 27] due to the importance of super-emitters in the methane budget[30]. The largest source observed was 145$\pm$36 t/hr and the smallest source was 0.6$\pm$0.2 t/hr, representing our best estimate of a detection limit.

# Persistent Methane Leaks from a Single Gas Field

Examination of the detected methane plumes shows persistent methane emissions. Fig. 2 shows methane plumes detected in a subregion within the Barsagelmez Oil Field (39.391°N, 53.833°E) near the Caspian Sea. We first observe methane plumes in 1987. With the exception of 1986, 1988, 2000, and 2002, we observe large methane plumes in this subregion nearly every year data is available. Specifically, we observe methane plumes emanating from three distinct locations within this subregion.

Fig. 2g shows the percentage of clear-sky scenes over this subregion that include a methane plume. Prior to the collapse of the USSR in 1991, we observe methane plumes in 0-20% of the clear sky scenes between 1986 and 1991. After the collapse, we observe methane plumes in 80-100% of the clear sky scenes between 1992 and 1999. This sharp increase in the frequency of plume detections coincides with the decline in Turkmenistan gas production starting in 1992 (Supplementary Information, Fig. S1). From 1994 to 1999 we observe a methane plume in more than 95% of the clear sky scenes. In other words, we observe 6 years of nearly continuous methane emissions from a single source. The start of these continuous methane emissions follows Russia's refusal to allow Turkmenistan to pass gas through Russian pipelines to Europe in 1994[31]. The situation was observed to improve in 2000 with only a single plume detected between 2000 and 2002. The frequency of plume detections increased again from 30% to 66% from 2008 to 2009 before being mitigated in 2011. Turkmen gas production declined in 2009 and 2010 due to the global financial crisis.

We calculated cumulative methane emissions from this subregion within the Barsagelmez Oil Field (Fig. 2g). From 1986 to 1992, the cumulative emissions increased at an average rate of 13.4 Gg per year. Beginning in 1992, when the persistent source was detected, the cumulative emissions increased by 80.1 Gg per year through 1999. Ultimately, we observe 0.73$\pm$0.13 Tg of methane released from this subregion between 1986 and 2000. The leakage detected from 2008 to 2011 add an additional 0.09 Tg, resulting in a lower bound on cumulative emissions of 0.82$\pm$0.16 Tg for this subregion from 1986 to 2011 (with missing data from 2001–2007). The total amount of methane released from the subregion is equivalent to a 0.30 ppb increase in the steady state atmospheric methane mixing ratio if it were instantaneously released, using a conversion factor[32] of 2.75 Tg $CH_4$ ppb$^{-1}$. The contribution to global mean methane concentrations is disproportionately large for just one subregion, indicating an important role of persistent point sources in the methane budget.

# National Emission Estimates from Turkmenistan

Fig. 3a shows the number of methane plume detections over Turkmenistan during the Landsat 5 observational period from 1986–2011. To account for the intermittent sampling and variations in cloud cover, we define the expected number of plume detections given perfect sampling as the coverage-adjusted detections: $p_C \equiv p_L \times n_I/n_L$, where $p_L$ is the number of plumes detected annually, $n_L$ is the number of clear-sky scenes in a year, and $n_I$ is the number of possible Landsat scenes over Turkmenistan in a year. Prior to the collapse of the USSR, we find 800-1000 coverage-adjusted plumes per year ($\sim$2.5 plumes/day). Both the number of detections and the coverage-adjusted detections increase in

1992 following the collapse of the USSR with the coverage adjusted plumes increasing by 29% to an average of 1230 plumes per year (3.4 plumes/day) between 1992 and 1999 with a maximum of 1600 plumes in 1994 (4.4 plumes/day).

Both the number of detected plumes and the coverage-adjusted plume detections are anti-correlated with the Turkmen natural gas production. After the USSR collapse, the dry natural gas production in Turkmenistan declined 77% from 57 billion cubic meters (BCM) in 1992 to the minimum of 13 BCM in 1998. We detected 84 methane plumes in Turkmenistan in 1998, the most of any year in the Landsat 5 record, when the Turkmenistan dry gas production was at a minimum. 1994 marked the maximum in the coverage-adjusted plume detections and, as mentioned above, Russia began refusing to allow Turkmenistan to pass gas through Russian pipelines to other markets in 1994[20]. We also observe an increase in plume detections in 2009–2010. This increase is coincident with a decline in Turkmen dry gas production following the global financial crisis in 2008.

One hypothesis for the increase in methane plume detections in the 1990s is that the socioeconomic decline following the USSR collapse reduced the frequency of maintenance and oversight, increasing the methane leakage from O&G operations. To assess this, we calculated methane emissions from each detected plume and estimated O&G leak rates (methane emitted per dry gas production) from 1986 to 2011. Extending the analysis from detected plumes to a national O&G emission estimate requires three assumptions: *i*) the statistics of the detected plumes are consistent with the true plume frequency, *ii*) the percent of O&G emissions coming from point sources is invariant, and *iii*) the point source emissions covary with national O&G emissions in Turkmenistan. The first assumption is necessitated by the low revisit frequency of Landsat 5 ($\sim$2 times per month), meaning that we do not detect all methane plumes. The latter assumption is because the detection limit of Landsat 5 precludes observing methane plumes smaller than 0.5 t/hr, meaning there are many O&G sources we do not detect. Following this, we compute the coverage-adjusted point source emissions by scaling the annual methane emissions from detected plumes by the ratio of the maximum possible Landsat scenes in a year to the number of clear-sky scenes. This yields an annual estimate for the point source emissions from Turkmenistan. To account for the sources below our detection limit, we compare our point source emissions to a bottom-up inventory prior to the USSR collapse. This allows us to determine the percent of O&G emissions our method can detect. The average emissions from point sources prior to the collapse was $183.4 \pm 22.6$ Gg/yr, which is $\sim$18% of the bottom-up O&G emissions for Turkmenistan[19]. Our point source emissions are scaled based on the average ratio between the bottom-up O&G emissions and the point source emissions between 1986 and 2000. We compute a lower bound assuming no scaling (i.e., the observed point source emissions represent all the O&G emissions) and the upper bound uses the largest ratio between 1986 and 2000. Finally, we assume the observed point source emissions covary with the national O&G emissions in Turkmenistan.

Fig. 3b shows the point source emissions and national gas leak rate in Turkmenistan over the Landsat 5 observational period. Point source emissions from O&G in Turkmenistan were $\sim$180 Gg/yr from 1986–1991. The emissions nearly triple to $463.2 \pm 215.7$ Gg/yr in 1994 and remain elevated through 1998 before declining to an average of $136.6 \pm 43.4$ Gg/yr from 2000–2002, similar to the pre-collapse level. The national leak rate in Turkmenistan was stable from 1986–1991 at 1–2%. This leak rate is comparable to many O&G basins in the United States[33, 34]. The leak rate exhibits a near-step change increase beginning in 1994 with a maximum of 10% in 1998. Upper bounds on the leak rate in 1994 and 1998 were 12% and 17%, respectively. The average leak rate from 1994 to 1998 was 6%, 4 times larger than the average pre-collapse leak rate. As with the detections, the leak rate is anti-correlated with the dry gas production throughout the record. We also observe an increase in the emissions and leak rate following the 2008 financial crisis.

# Implications for the Methane Budget

Our work finds an anti-correlation between the dry gas production and methane emissions from O&G operations in Turkmenistan from 1986–2011. While the focus of our analysis was on Turkmenistan, the work likely has implications for the broader USSR as bottom-up inventories attribute half of the change in USSR emissions to Turkmenistan. We observe an increase in methane plume detections, O&G emissions, and the leak rate from Turkmenistan O&G in 1992 after the collapse of the USSR. The two maximum leak rates occur in 1994 and 1998. These maxima coincide with geopolitical and economic events during this period of turmoil: Russia began refusing to transmit Turkmen gas to other markets in 1994 and Turkmenistan's dry gas production was at a minimum in 1998. Our results suggest that the socioeconomic turmoil following the USSR collapse resulted in widespread infrastructure failure, large methane leaks from O&G operations, and an increase in methane emissions in the 1990s. As such, we find it unlikely that the methane slowdown in the 1990s was caused by the collapse of the USSR. This is in contrast to previous work attributing the methane slowdown to the collapse of the USSR due to decreased gas production[1, 2, 4]. Our results beg the question: *"what drove the methane slowdown in the 1990s?"*

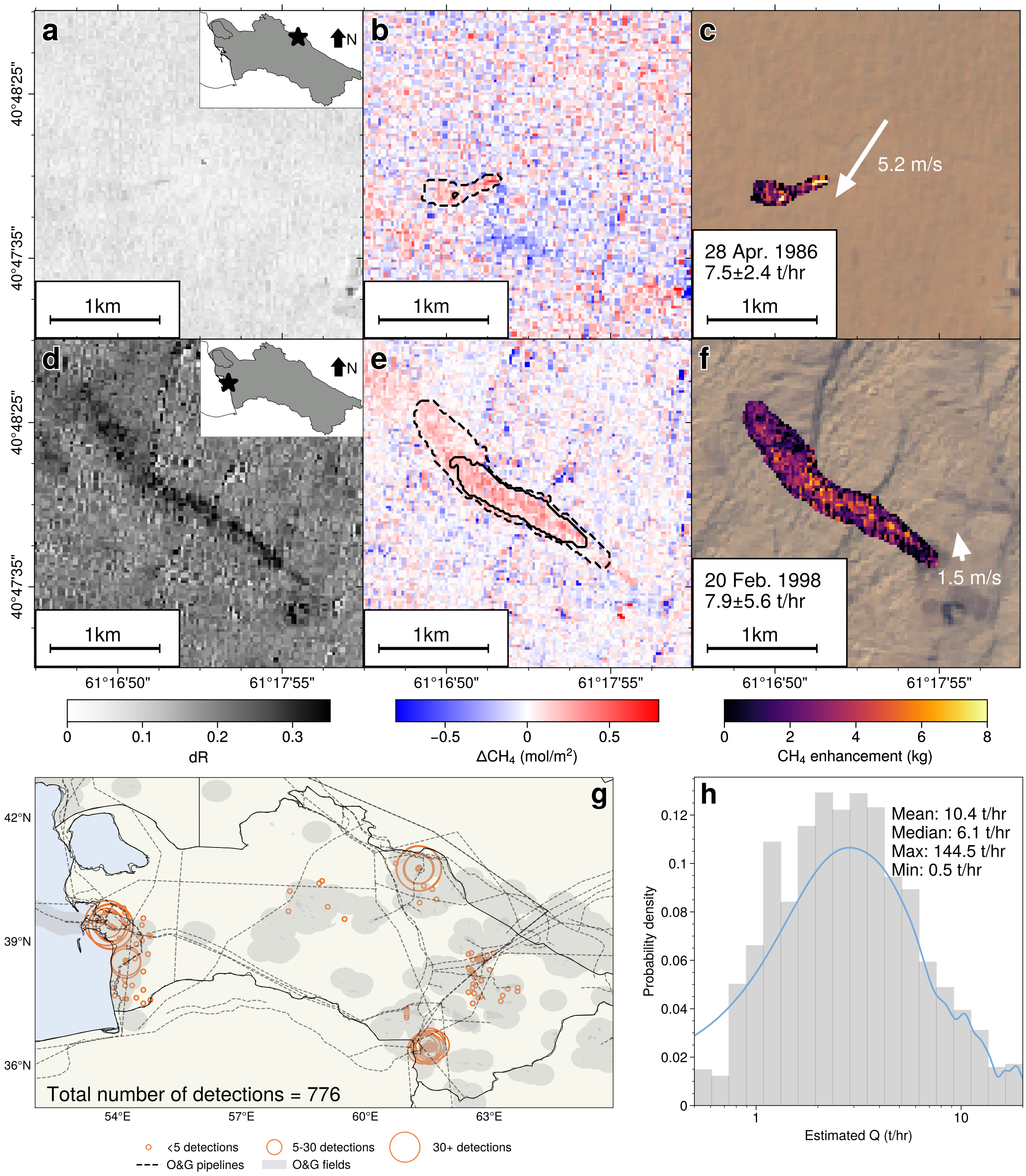


Figure 1: **Detection of methane plumes in Turkmenistan from 1986 to 2011.** (Panels a-c) Fractional differences in SWIR top-of-atmosphere reflectances ($dR$), retrieved methane column anomalies, and estimated methane enhancements, respectively, for one of the oldest methane plumes detected in Turkmenistan from Landsat 5. (Panels d-f) Same as panels a-c, but for another methane plume. Dashed plume contours are with low confidence levels and solid contours are for the high confidence regions. (Panel g) Location of detected methane plumes. (Panel h) Histogram of the methane emissions for the detected plumes.

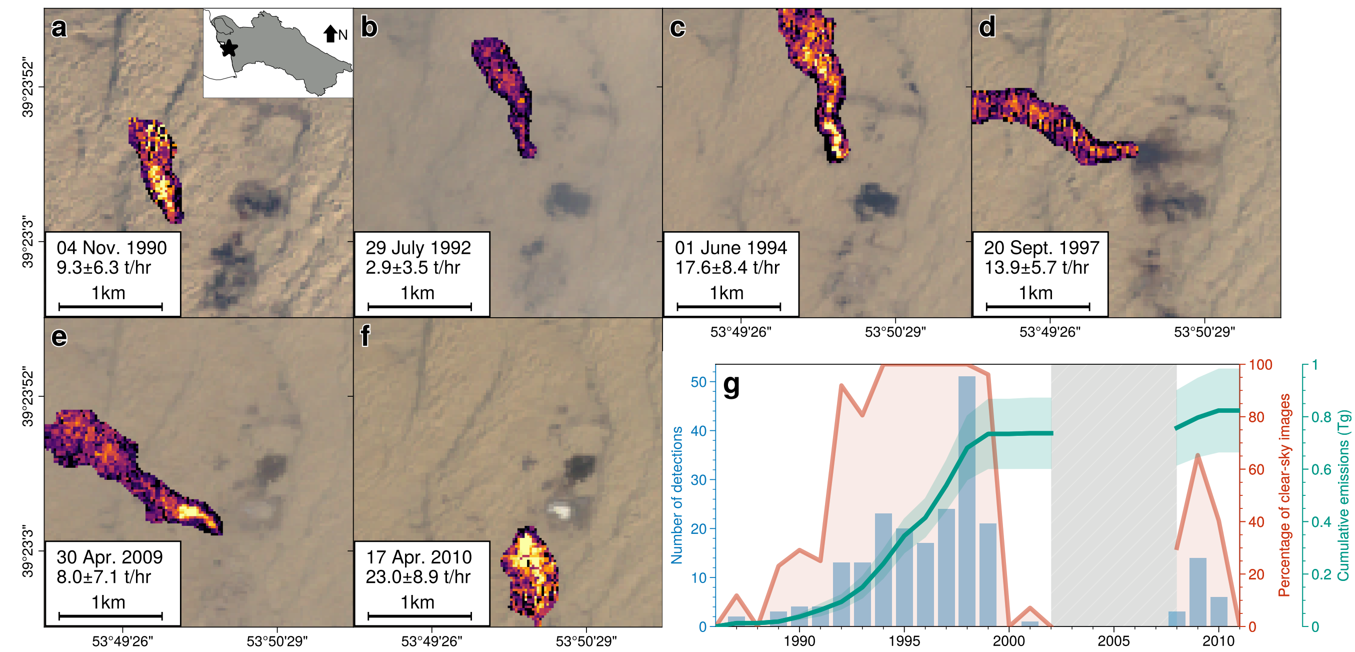


Figure 2: **Persistent regional methane emissions from the Barsagelmez Oil Field.** (Panels a-f) Example methane plumes from the Barsagelmez Oil Field (39.391°N, 53.833°E) from 1986–2011. (Panel g) number of detections (light blue), percent of clear-sky scenes with detections (orange), and estimated cumulative emissions from this source (teal). Gray shaded area indicates years with no Landsat 5 images available on Google Earth Engine due to the decentralized handling and distribution of Landsat 5 data sets.

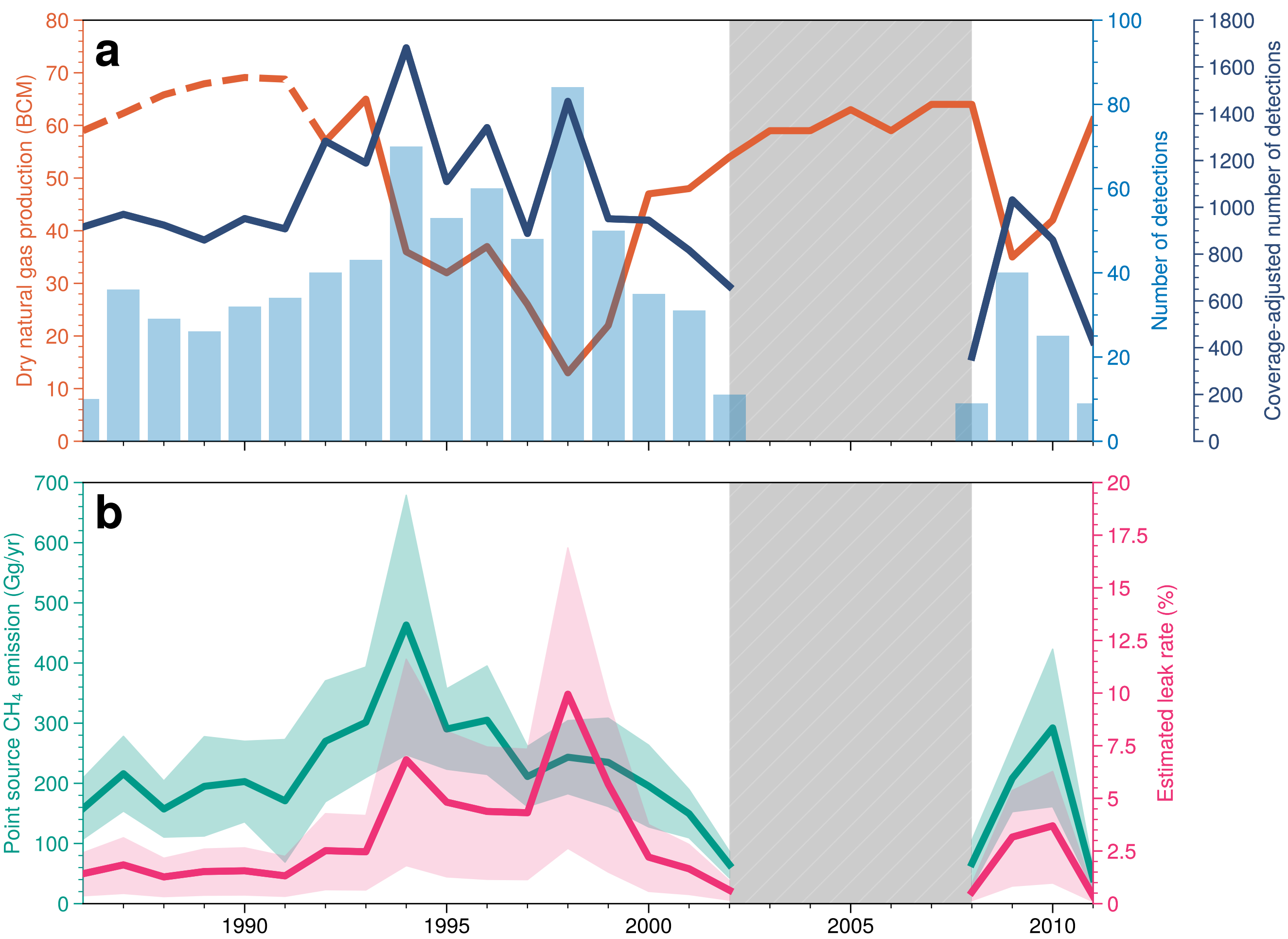


Figure 3: **Time series analysis of methane point sources detected in Turkmenistan.** (Panel a) Number of detected methane plumes per year (light blue), the EIA dry natural gas production[18] (orange), and coverage-adjusted number of detections (dark blue). Dashed orange line between 1986 and 1991 indicates dry natural gas production estimated based on scaling using EDGAR O&G emissions. (Panel b) Estimated annual methane emissions from the point sources (teal) and estimated national O&G leak rate in Turkmenistan (pink). Gray shaded area indicates years with no Landsat 5 images available on Google Earth Engine due to the decentralized handling and distribution of Landsat 5 data sets.

# Method

In this study, we trained an ensemble of deep learning models to detect methane plumes and predict plume masks from images sampled by Sentinel-2 and Landsat satellites. All the models are trained using human-annotated plume masks labelled following the literature. The ensemble is used to search for historical methane plumes in Landsat 5 data sets over Turkmenistan. The plume masks predicted by the ensemble are used to quantify methane emission rates using the integrated methane enhancement (IME) method. Uncertainties on the estimated flux rates are calculated and provided.

## Deep Learning Model

The deep learning model we use is adapted from the U-net model, which was originally proposed for biomedical segmentation problems[35]. The U-net model has been recently widely applied in the field of earth science[36, 37, 38, 39]. The schematic diagram of the model architecture is shown in Fig. S2 in the Supplementary Information. The U-net model is an encoder-decoder and is constructed based on the convolutional neural networks (CNN)[40]. The first half of the model is an encoder, in which the vectors of input information are filtered by 2-dimensional kernels in each convolutional layer and the dimensions of the intermediate outputs (also called latent vectors) are reduced by max-pooling layers. The second half of the model is a decoder that up-samples the compressed latent vectors to the model output layer. The up-sampling process is done via convolutional layers and transposed convolutional layers. During the training process, the model predictions are compared against the ground truth, and the differences between the truth and model predictions are used to calculate partial gradients to optimize the convolutional kernels in the model. Compared to the classic U-net model, we replaced the encoder half with the ResNeXt-50 model, which is a more efficient model to extract patterns from images[41]. We applied transfer learning by using the pre-trained ResNeXt-50 model weights before each training process to boost the convergence of training and improve final model performance.

## Input and Output Variables

Methane absorbs strongly around the 1.6 $\mu$m and 2.2 $\mu$m bands in the shortwave infrared (SWIR), which is measured by Landsat 4-9 and Sentinel-2A/B satellites. We hereafter denote the measured reflectance in the 1.6 $\mu$m and 2.2 $\mu$m bands as $R_{11}$ and $R_{12}$, respectively, following the Sentinel-2 convention. Following the Multi-Band-Single-Pass method[21], we define the following quantity, $dR$, to capture methane enhancements:

$$dR = \frac{cR_{12} - R_{11}}{R_{11}}$$

where $c$ denotes the scaling factor to account for the overall brightness difference between the two bands. The $dR$ quantity could be used for the retrieval of methane concentrations by fitting a radiative transfer model[42, 21].

The input variables for the deep learning model include $dR$, an estimate of the background $dR$, the grey-scale RGB image, the normalized difference vegetation index (NDVI), and two $\Delta dR$ fields representing differences between $dR$ and the background $dR$. NDVI is a classic remote sensing index capturing vegetation on land surface, which is defined as follows:

$$\text{NDVI} = \frac{R_{NIR} - R_{red}}{R_{NIR} + R_{red}}$$

Here, $R_{NIR}$ and $R_{red}$ denote the measured reflectance in the near-infrared (NIR) and red bands. The background $dR$ is estimated by averaging $dR$ with structural similarity indices (SSIM) higher than 0.5 within ±180 days from the target scene. SSIM is a metric used frequently in computer vision to measure the similarity between two images, which accounts for image texture and is indicative of the perceived similarity. SSIM is defined by the following equation:

$$SSIM = \frac{(2\mu_x\mu_y + (k_1L)^2)(2\sigma_{xy} + (k_2L)^2)}{(\mu_x^2 + \mu_y^2 + (k_1L)^2)(\sigma_x^2 + \sigma_y^2 + (k_2L)^2)}$$

where $\mu_i$ and $\sigma_i$ stand for the mean and standard deviation of the pixels of the corresponding images, respectively. $\sigma_{xy}$ is the covariance between the two images. $k_1 = 0.01$, $k_2 = 0.03$, and $L = 2\ bit\ px^{-1} - 1$ are variables for the stabilization of the index. The first $\Delta dR$ field, $\Delta dR_1$, is defined by the following equation:

$$\Delta dR_1 = Z(dR - c' dR_{bg})$$

where $c'$ adjusts the brightness difference between the target scene and the background scene, and $Z$ stands for the standard score calculation. The second $\Delta dR$ field, $\Delta dR_2$, is the Z-score of the difference between $dR$ of the target scene and the raw background $dR$.

The output of the deep learning model is binary masks of methane plumes. We use human-annotated plume masks, following the literature, using a customized graphical user interface (GUI). Fig. S3 in the Supplementary Information shows the panel of the GUI. Each methane plume was annotated by more than one person, which is helpful for preventing overfitting data from a single labeller. The data labelling was done following the literature about reported recent detected methane plumes. Overall, we labelled 663 methane plumes as the positive data set, and we labelled 969 satellite scenes without any plumes as the negative data set. These numbers are low for data-driven methods, so we applied augmentation steps to increase the volume of training data set. As shown in Fig. S4, the augmentation steps include 90° rotation, horizontal and vertical flip, and addition of 10% Gaussian noise. These augmentation steps are randomly applied for each augmented data sample. We add 10% Gaussian noise to improve the robustness of deep learning models against the noise in Landsat 5 data sets. As shown in Fig. S6, the final training set contains 3313 positive samples and 4831 negative samples after the augmentation process.

### Training Details and Construction of the Ensemble

The loss function we use during the training process is a multi-term loss, which is defined as follows:

$$L = -\sum_i (y_i \ln \hat{y}_i + (1 - y_i) \ln(1 - \hat{y}_i))) + (1 - \frac{2|Y \cap \hat{Y}|}{|Y| + |\hat{Y}|})$$

Here, $y_i$ and $\hat{y}_i$ represent true labels and predicted labels for each pixel, respectively. $Y$ and $\hat{Y}$ stand for the whole set of true labels and predicted labels, respectively. The first term is the binary cross entropy (BCE) loss, which is popularly used in binary classification problems and is derived by maximizing the likelihood of correctly predicting the binary labels. The second term is the loss from the Dice score. The Dice score calculates the fraction of the overlap between the two sets of true labels and predicted labels over both sets, which measures the overall correctness of mask segmentation. We use the Adam optimization algorithm for the convergence of the training. Training of deep learning model is conducted using NVIDIA A2 Tensor Core GPUs.

Instead of one model, we trained 20 realizations of the deep learning model. The application of ensemble of deep learning models is useful for the quantification of uncertainties in the predicted methane plume masks[43]. As shown in the schematic diagram in Fig. S5, each deep learning model is trained using a subset of the training data set. During the training of each ensemble member, the hyper-parameters associated with training are randomly perturbed. Details about the hyper-parameters are shown in Table S1 in the Supplementary Information.

### Quantification of Methane Emission Rates and Uncertainty

We use the integrated methane enhancement (IME) method to quantify emission rates of the detected methane point sources[25] and the uncertainties. The flux rate of a point source could be estimated using the following equation:

$$Q = \frac{U_{eff}}{L} \sum_{j=1}^{N} \Delta\Omega_j A_j$$

where $U_{eff}$ is the effective wind speed, $L$ is the plume size, $\Delta\Omega_j$ represents the methane enhancement in each pixel, and $A_j$ stands for the pixel size. We estimate $L$ to be square root of the area of the plume mask. The effective wind speed is calculated using the empirical relationship between $U_{eff}$ and 10m wind speed[21]:

$$U_{eff} = \alpha U_{10m} + \beta$$

where $\alpha = 0.33$ and $\beta = 0.45\text{ms}^{-1}$.

The uncertainty on $Q$ is estimated using the following equation:

$$\delta Q \simeq \sqrt{\left(\frac{Q\delta U_{eff}}{U_{eff}}\right)^2 + \left(\frac{Q\delta L}{L}\right)^2 + \left(\frac{U_{eff}\delta\Delta\Omega_j}{L}\sum_{j=1}^{N} A_j\right)^2}$$

To propagate the uncertainty on $Q$, we use an absolute error of 2 m/s for $U_{10m}$ and a 20% uncertainty on the plume size ($\sum_j A_j$). For the uncertainty on pixel-wise methane enhancement, we estimate $\delta\Delta\Omega_j$ to be the standard error calculated using all pixels outside the plume mask.

## Data, Materials, and Software Availability

The annotation of methane plumes involves multispectral top-of-atmosphere (TOA) reflectance measurements from Landsat 8 and Sentinel-2, which are available publicly from Google Earth Engine (GEE, `https://developers.google.com/earth-engine/datasets`). Landsat 5 TOA reflectance measurements are also from Google Earth Engine, which can be accessed using the GEE Python API (`https://developers.google.com/earth-engine/tutorials/community/intro-to-python-api`). Dry natural gas production data could be accessed from the U.S. Energy Information Administration (EIA) website (`https://www.eia.gov/international/data/country/TKM/natural-gas/dry-natural-gas-production`). The Emissions Database for Global Atmospheric Research (EDGAR) version 7.0 GHG emission inventory could be accessed from: `https://edgar.jrc.ec.europa.eu/dataset_ghg70`.

The deep learning model was implemented using PyTorch (https://pytorch.org/). The code for the methane plume mask annotation tool is available at `https://github.com/tailonghe/methane_labeller`. The code to reproduce results in this paper is available at `https://github.com/tailonghe/L5_methane_detection`. The methane column retrieval code will be made available for non-commercial use upon request (Copyright © 2021 GHGSAT Inc). The code includes the code to train deep learning models, the code to construct the ensemble system, the scripts to download and process Landsat images from GEE and the code to detect and quantify methane plumes.


## Acknowledgements

T.L.H. and R.J.B. were supported by a NASA Early Career Faculty Grant (80NSSC21K1808) to A.J.T. This research is supported in part by the generosity of Eric and Wendy Schmidt by recommendation of Schmidt Futures, as part of its Virtual Earth System Research Institute (VESRI), and through computational resources funded by the Environmental Defense Fund.

# Supplementary Information

This supplementary information includes 7 additional figures and a table discussed in the main text. Fig. S1 shows EDGAR methane emissions associated with O&G productions, compared between the USSR and Turkmenistan. Fig. S2 shows the schematic diagram of the U-net model to predict methane plume mask using Landsat 5 multi-spectral images. Fig. S3 shows the panel of the graphical user interface (GUI) used for labelling methane plumes from the literature. Fig. S4 illustrates the augmentation steps applied to enrich the training data set. Fig. S5 shows the construction and the application of the ensemble of U-net models. Table 1 shows the hyperparameters associated with the training of each ensemble member. Fig. S6 shows the statistics about the original human-labelled training data set and the augmented data set. Fig. S7 shows the comparison between reported flux rates from [23, 25, 22] and the corresponding flux rates estimated by our system.

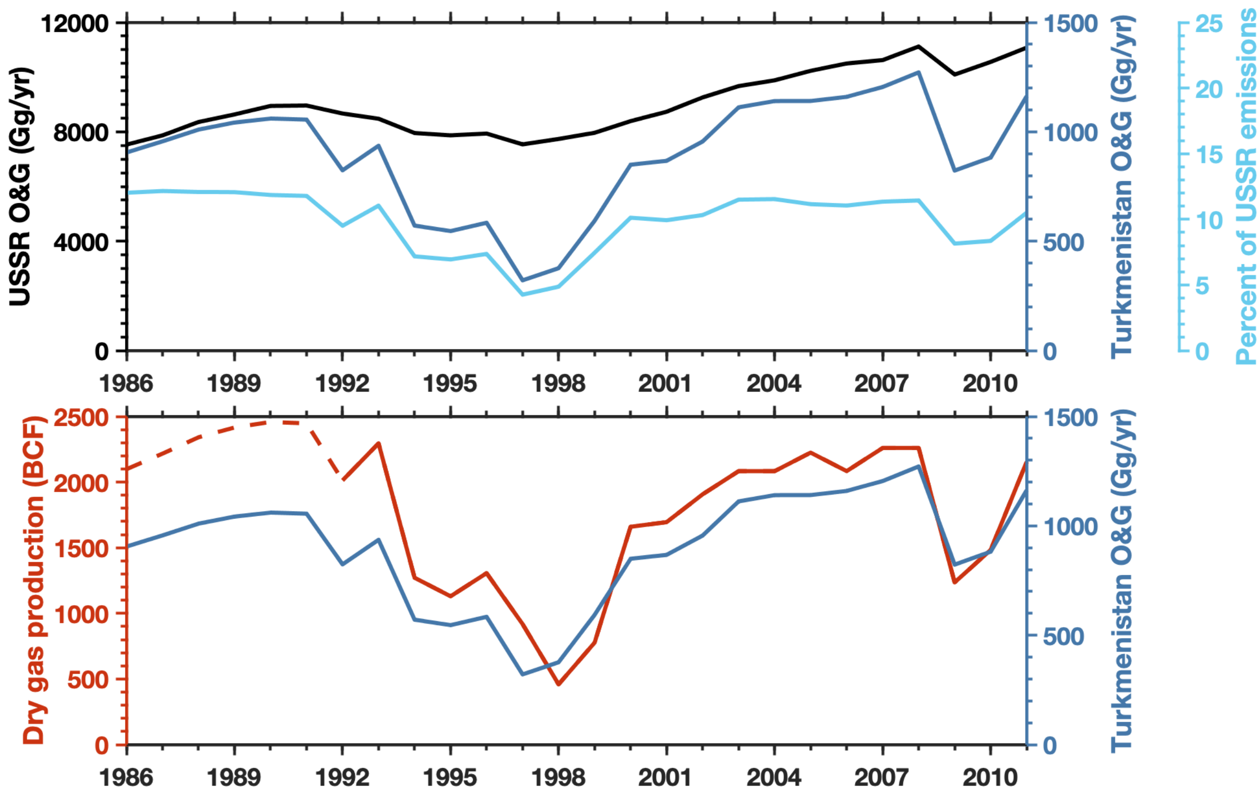


Figure S4: **Variations in EDGAR methane emissions and Turkmenistan dry natural gas production.** (Top) EDGAR methane emissions from O&G production for the former USSR (black) and Turkmenistan (dark blue). Turkmenistan's percent of the USSR methane emissions is shown in light blue. (Bottom) Dry gas production in Turkmenistan (red) and the EDGAR O&G methane emissions for Turkmenistan (dark blue). The dashed line between 1986 and 1991 indicates dry natural gas production estimated based on scaling using EDGAR O&G emissions.

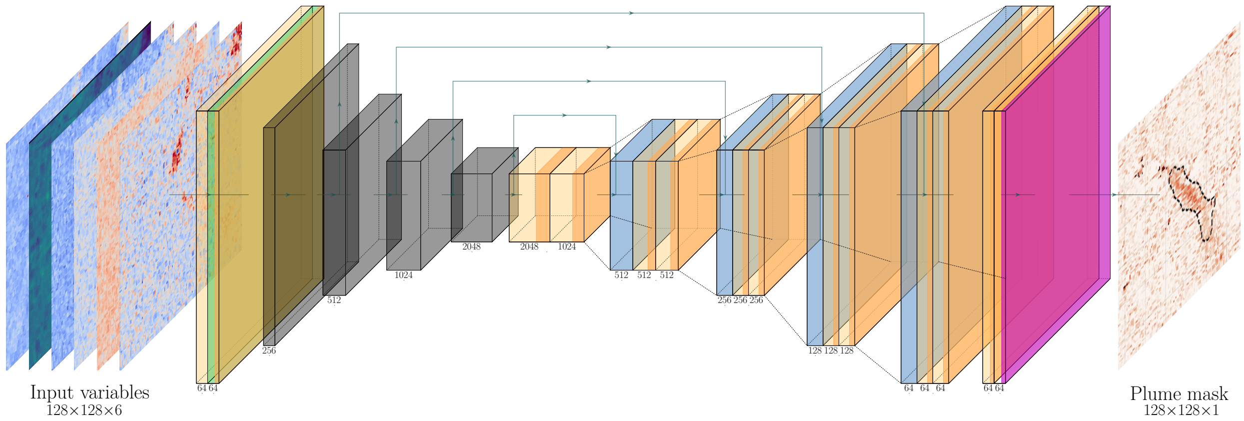


Figure S5: **Schematic diagram of the U-net model architecture.** Grey boxes are the ResNeXt-50 (32×4d) pretrained model blocks. Light orange and light blue boxes represent convolutional layers and up-convolutional layers. The green box is batch normalization layer, dark orange layers are Rectified Linear Unit (ReLU) activation layers, and the last magenta layer is sigmoid activation layer.

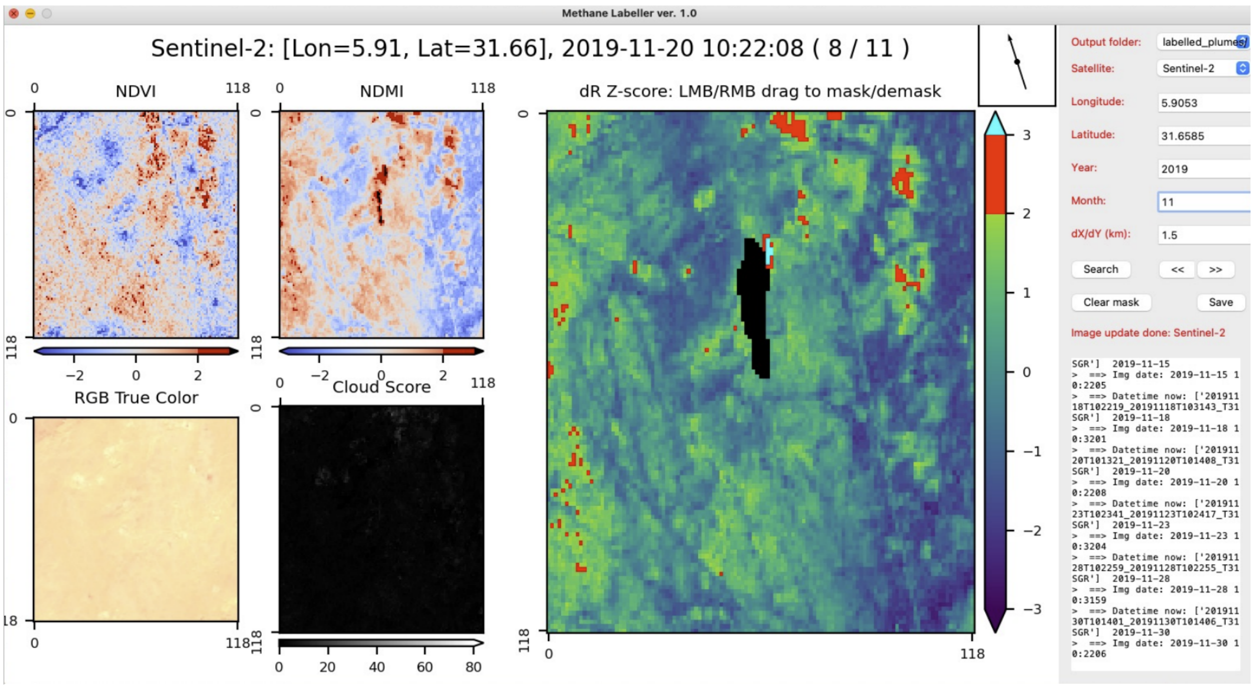


Figure S6: Panel of the graphical user interface (GUI) for labelling methane plumes from the literature.

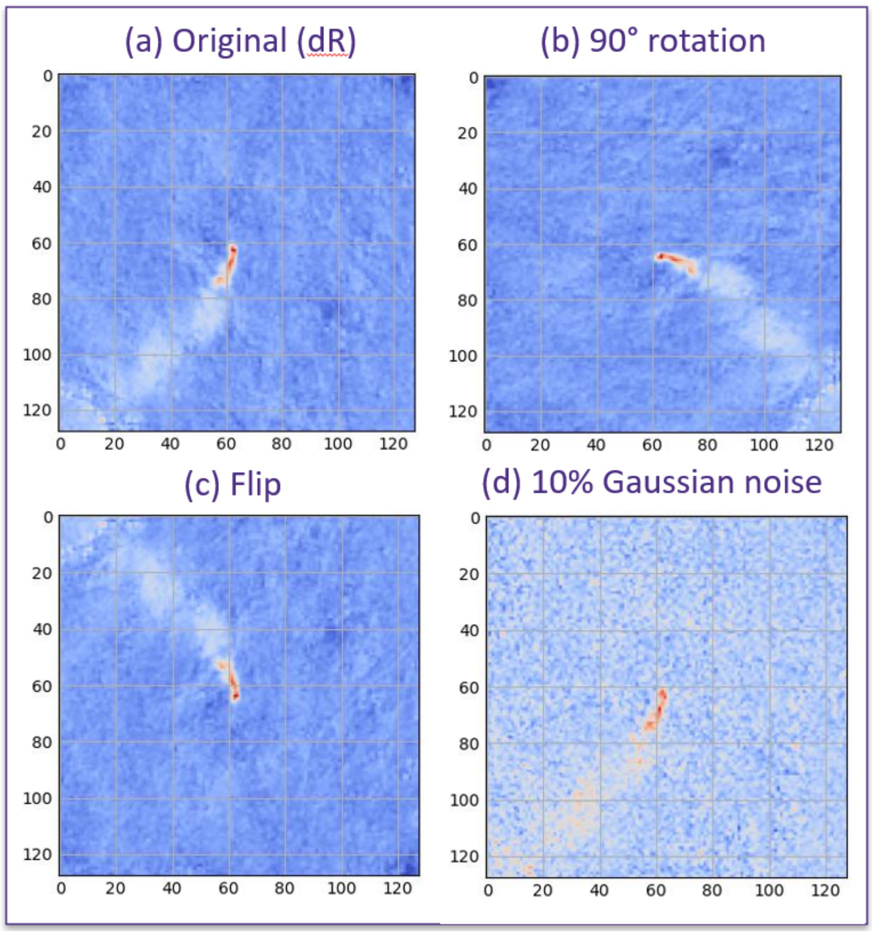


Figure S7: Augmentation steps applied on the training data set.

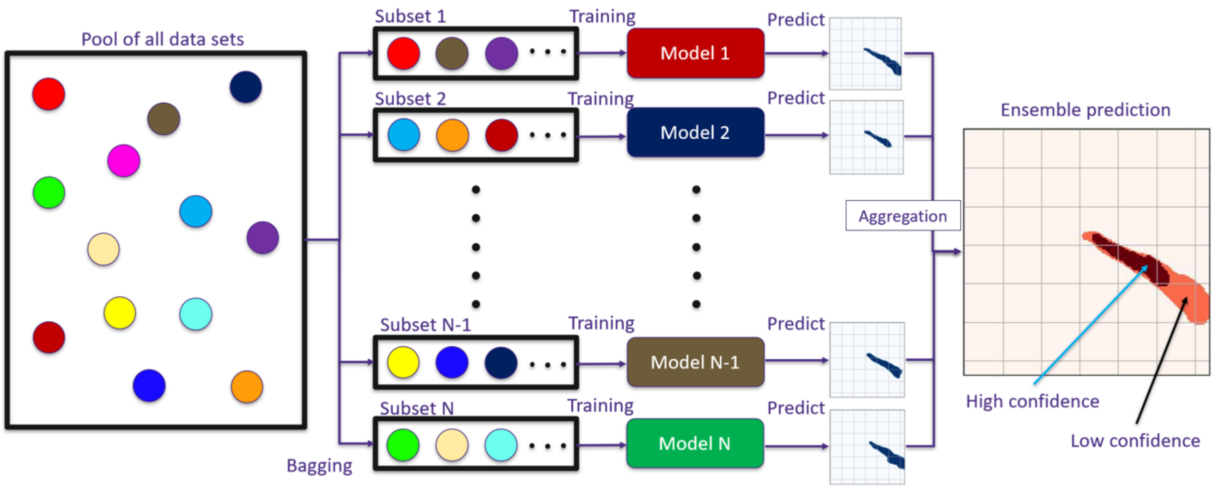


Figure S8: Schematic diagram of the construction and the application of the ensemble of U-net models.

Table S1: Hyperparameters associated with training of each U-net model in the ensemble.

| Ensemble number | Learning rate | Batch size | Number of epoch |
|---|---|---|---|
| 1 | 1.55e-4 | 8 | 33 |
| 2 | 1.21e-4 | 10 | 26 |
| 3 | 1.26e-4 | 9 | 30 |
| 4 | 1.05e-4 | 10 | 25 |
| 5 | 1.97e-4 | 9 | 33 |
| 6 | 1.24e-4 | 14 | 27 |
| 7 | 1.58e-4 | 8 | 32 |
| 8 | 1.31e-4 | 12 | 27 |
| 9 | 1.49e-4 | 5 | 31 |
| 10 | 1.00e-4 | 5 | 27 |
| 11 | 1.53e-4 | 14 | 34 |
| 12 | 1.85e-4 | 14 | 30 |
| 13 | 1.28e-4 | 13 | 34 |
| 14 | 1.90e-4 | 12 | 33 |
| 15 | 8.68e-5 | 11 | 28 |
| 16 | 8.35e-5 | 6 | 31 |
| 17 | 9.98e-4 | 6 | 31 |
| 18 | 9.90e-5 | 5 | 33 |
| 19 | 1.82e-4 | 13 | 26 |
| 20 | 1.88e-4 | 13 | 31 |

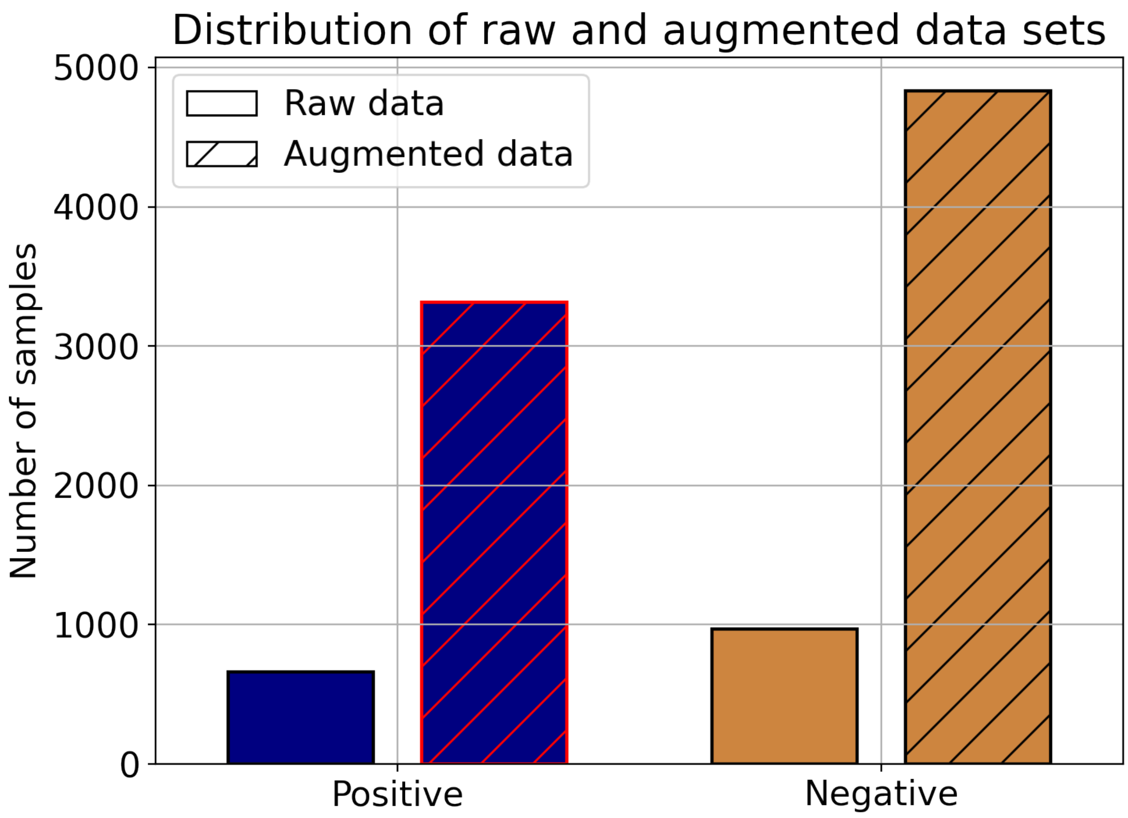


Figure S9: Statistics about the original labelled data sets and the augmented data sets.

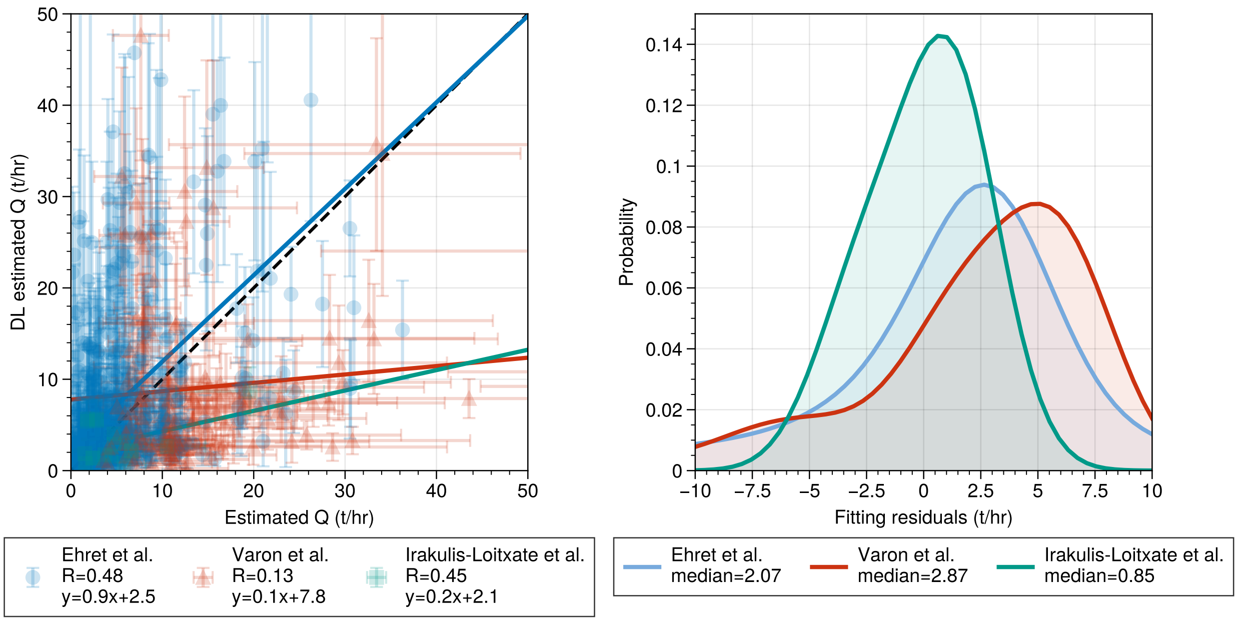


Figure S10: Validation of the flux rates estimated using our system and other studies from the literature. (a) shows the correlation between the reported flux rates from [23, 25, 22] and our corresponding estimates. (b) shows the distribution of the residuals from linear regression in (a).

# References


[1] E. J. Dlugokencky et al. "A dramatic decrease in the growth rate of atmospheric methane in the northern hemisphere during 1992". In: *Geophysical Research Letters* 21.1 (1994), pp. 45–48. DOI: `https://doi.org/10.1029/93GL03070`. eprint: `https://agupubs.onlinelibrary.wiley.com/doi/pdf/10.1029/93GL03070`. URL: `https://agupubs.onlinelibrary.wiley.com/doi/abs/10.1029/93GL03070`.

[2] E. J. Dlugokencky et al. "Atmospheric methane levels off: Temporary pause or a new steady-state?" In: *Geophysical Research Letters* 30.19 (2003). DOI: `https://doi.org/10.1029/2003GL018126`. eprint: `https://agupubs.onlinelibrary.wiley.com/doi/pdf/10.1029/2003GL018126`. URL: `https://agupubs.onlinelibrary.wiley.com/doi/abs/10.1029/2003GL018126`.

[3] M. Rigby et al. "Renewed growth of atmospheric methane". In: *Geophysical Research Letters* 35.22 (2008). DOI: `https://doi.org/10.1029/2008GL036037`. eprint: `https://agupubs.onlinelibrary.wiley.com/doi/pdf/10.1029/2008GL036037`. URL: `https://agupubs.onlinelibrary.wiley.com/doi/abs/10.1029/2008GL036037`.

[4] Hinrich Schaefer et al. "A 21st-century shift from fossil-fuel to biogenic methane emissions indicated by $^{13}CH_4$". In: *Science* 352.6281 (2016), pp. 80–84. DOI: `10.1126/science.aad2705`. eprint: `https://www.science.org/doi/pdf/10.1126/science.aad2705`. URL: `https://www.science.org/doi/abs/10.1126/science.aad2705`.

[5] Stefan Schwietzke et al. "Upward revision of global fossil fuel methane emissions based on isotope database". In: *Nature* 538.7623 (2016), pp. 88–91. ISSN: 1476-4687. DOI: `10.1038/nature19797`. URL: `https://doi.org/10.1038/nature19797`.

[6] Alexander J. Turner et al. "Ambiguity in the causes for decadal trends in atmospheric methane and hydroxyl". In: *Proceedings of the National Academy of Sciences* 114.21 (2017), pp. 5367–5372. DOI: `10.1073/pnas.1616020114`. eprint: `https://www.pnas.org/doi/pdf/10.1073/pnas.1616020114`. URL: `https://www.pnas.org/doi/abs/10.1073/pnas.1616020114`.

[7] Alexander J. Turner et al. "Modulation of hydroxyl variability by ENSO in the absence of external forcing". In: *Proceedings of the National Academy of Sciences* 115.36 (2018), pp. 8931–8936. DOI: `10.1073/pnas.1807532115`. eprint: `https://www.pnas.org/doi/pdf/10.1073/pnas.1807532115`. URL: `https://www.pnas.org/doi/abs/10.1073/pnas.1807532115`.

[8] Matthew Rigby et al. "Role of atmospheric oxidation in recent methane growth". In: *Proceedings of the National Academy of Sciences* 114.21 (2017), pp. 5373–5377. DOI: `10.1073/pnas.1616426114`. eprint: `https://www.pnas.org/doi/pdf/10.1073/pnas.1616426114`. URL: `https://www.pnas.org/doi/abs/10.1073/pnas.1616426114`.

[9] John R. Worden et al. "Reduced biomass burning emissions reconcile conflicting estimates of the post-2006 atmospheric methane budget". In: *Nature Communications* 8.1 (2017), p. 2227. ISSN: 2041-1723. DOI: `10.1038/s41467-017-02246-0`. URL: `https://doi.org/10.1038/s41467-017-02246-0`.

[10] Alexander J. Turner, Christian Frankenberg, and Eric A. Kort. "Interpreting contemporary trends in atmospheric methane". In: *Proceedings of the National Academy of Sciences* 116.8 (2019), pp. 2805–2813. DOI: `10.1073/pnas.1814297116`. eprint: `https://www.pnas.org/doi/pdf/10.1073/pnas.1814297116`. URL: `https://www.pnas.org/doi/abs/10.1073/pnas.1814297116`.

[11] E. G. Nisbet et al. “Very Strong Atmospheric Methane Growth in the 4 Years 2014–2017: Implications for the Paris Agreement”. In: *Global Biogeochemical Cycles* 33.3 (2019), pp. 318–342. DOI: https://doi.org/10.1029/2018GB006009. eprint: https://agupubs.onlinelibrary.wiley.com/doi/pdf/10.1029/2018GB006009. URL: https://agupubs.onlinelibrary.wiley.com/doi/abs/10.1029/2018GB006009.

[12] Newton H. Nguyen et al. “Effects of Chemical Feedbacks on Decadal Methane Emissions Estimates”. In: *Geophysical Research Letters* 47.3 (2020). e2019GL085706 10.1029/2019GL085706, e2019GL085706. DOI: https://doi.org/10.1029/2019GL085706. eprint: https://agupubs.onlinelibrary.wiley.com/doi/pdf/10.1029/2019GL085706. URL: https://agupubs.onlinelibrary.wiley.com/doi/abs/10.1029/2019GL085706.

[13] Joshua L. Laughner et al. “Societal shifts due to COVID-19 reveal large-scale complexities and feedbacks between atmospheric chemistry and climate change”. In: *Proceedings of the National Academy of Sciences* 118.46 (2021), e2109481118. DOI: 10.1073/pnas.2109481118. eprint: https://www.pnas.org/doi/pdf/10.1073/pnas.2109481118. URL: https://www.pnas.org/doi/abs/10.1073/pnas.2109481118.

[14] D. S. Stevenson et al. “COVID-19 lockdown emission reductions have the potential to explain over half of the coincident increase in global atmospheric methane”. In: *Atmospheric Chemistry and Physics* 22.21 (2022), pp. 14243–14252. DOI: 10.5194/acp-22-14243-2022. URL: https://acp.copernicus.org/articles/22/14243/2022/.

[15] Shushi Peng et al. “Wetland emission and atmospheric sink changes explain methane growth in 2020”. In: *Nature* 612.7940 (2022), pp. 477–482. ISSN: 1476-4687. DOI: 10.1038/s41586-022-05447-w. URL: https://doi.org/10.1038/s41586-022-05447-w.

[16] L. Feng et al. “Methane emissions are predominantly responsible for record-breaking atmospheric methane growth rates in 2020 and 2021”. In: *Atmospheric Chemistry and Physics* 23.8 (2023), pp. 4863–4880. DOI: 10.5194/acp-23-4863-2023. URL: https://acp.copernicus.org/articles/23/4863/2023/.

[17] O. B. Dimdore-Miles, P. I. Palmer, and L. P. Bruhwiler. “Detecting changes in Arctic methane emissions: limitations of the inter-polar difference of atmospheric mole fractions”. In: *Atmospheric Chemistry and Physics* 18.24 (2018), pp. 17895–17907. DOI: 10.5194/acp-18-17895-2018. URL: https://acp.copernicus.org/articles/18/17895/2018/.

[18] U.S. Energy Information Agency (EIA). *Turkmenistan Production and Consumption of Dry Natural Gas*. https://www.eia.gov/international/data/country/TKM/infographic/natural-gas-infographic. Accessed July 28, 2023.

[19] EDGAR - Emissions Database for Global Atmospheric Research. *Global Greenhouse Gas Emissions: EDGAR v7.0*. https://edgar.jrc.ec.europa.eu/dataset_ghg70. Accessed July 28, 2023.

[20] International Monetary Fund. *Turkmenistan: Recent Economic Developments*. https://www.elibrary.imf.org/view/journals/002/1998/081/article-A001-en.xml. USA, 1998. DOI: 10.5089/9781451837230.002.A001.

[21] D. J. Varon et al. “High-frequency monitoring of anomalous methane point sources with multispectral Sentinel-2 satellite observations”. In: *Atmospheric Measurement Techniques* 14.4 (2021), pp. 2771–2785. DOI: 10.5194/amt-14-2771-2021. URL: https://amt.copernicus.org/articles/14/2771/2021/.

[22] Itziar Irakulis-Loitxate et al. “Satellite-based survey of extreme methane emissions in the Permian basin”. In: *Science Advances* 7.27 (2021), eabf4507. DOI: 10.1126/sciadv.abf4507. eprint: https://www.science.org/doi/pdf/10.1126/sciadv.abf4507. URL: https://www.science.org/doi/abs/10.1126/sciadv.abf4507.

[23] Thibaud Ehret et al. “Global Tracking and Quantification of Oil and Gas Methane Emissions from Recurrent Sentinel-2 Imagery”. In: *Environmental Science & Technology* 56.14 (2022). PMID: 35797726, pp. 10517–10529. DOI: 10.1021/acs.est.1c08575. eprint: https://doi.org/10.1021/acs.est.1c08575. URL: https://doi.org/10.1021/acs.est.1c08575.

[24] Christian Frankenberg et al. “Airborne methane remote measurements reveal heavy-tail flux distribution in Four Corners region”. In: *Proceedings of the National Academy of Sciences* 113.35 (2016), pp. 9734–9739. DOI: 10.1073/pnas.1605617113. eprint: https://www.pnas.org/doi/pdf/10.1073/pnas.1605617113. URL: https://www.pnas.org/doi/abs/10.1073/pnas.1605617113.

[25] D. J. Varon et al. “Quantifying methane point sources from fine-scale satellite observations of atmospheric methane plumes”. In: *Atmospheric Measurement Techniques* 11.10 (2018), pp. 5673–5686. DOI: 10.5194/amt-11-5673-2018. URL: https://amt.copernicus.org/articles/11/5673/2018/.

[26] Hans Hersbach et al. “The ERA5 global reanalysis”. In: *Quarterly Journal of the Royal Meteorological Society* 146.730 (2020), pp. 1999–2049. DOI: https://doi.org/10.1002/qj.3803. eprint: https://rmets.onlinelibrary.wiley.com/doi/pdf/10.1002/qj.3803. URL: https://rmets.onlinelibrary.wiley.com/doi/abs/10.1002/qj.3803.

[27] T. Lauvaux et al. “Global assessment of oil and gas methane ultra-emitters”. In: *Science* 375.6580 (2022), pp. 557–561. DOI: 10.1126/science.abj4351. eprint: https://www.science.org/doi/pdf/10.1126/science.abj4351. URL: https://www.science.org/doi/abs/10.1126/science.abj4351.

[28] Itziar Irakulis-Loitxate et al. “Satellites Detect Abatable Super-Emissions in One of the World’s Largest Methane Hotspot Regions”. In: *Environmental Science & Technology* 56.4 (2022). PMID: 35102741, pp. 2143–2152. DOI: 10.1021/acs.est.1c04873. eprint: https://doi.org/10.1021/acs.est.1c04873. URL: https://doi.org/10.1021/acs.est.1c04873.

[29] Riley M. Duren et al. "California's methane super-emitters". In: *Nature* 575.7781 (Nov. 2019), pp. 180–184. ISSN: 1476-4687. DOI: 10.1038/s41586-019-1720-3. URL: https://doi.org/10.1038/s41586-019-1720-3.

[30] A. R. Brandt et al. "Methane Leaks from North American Natural Gas Systems". In: *Science* 343.6172 (2014), pp. 733–735. DOI: 10.1126/science.1247045. eprint: https://www.science.org/doi/pdf/10.1126/science.1247045. URL: https://www.science.org/doi/abs/10.1126/science.1247045.

[31] U.S. Department of State. *Previous Editions of Turkmenistan Background Note: Turkmenistan (01/01)*. https://2009-2017.state.gov/outofdate/bgn/turkmenistan/14925.htm. Accessed July 28, 2023.

[32] Michael J. Prather, Christopher D. Holmes, and Juno Hsu. "Reactive greenhouse gas scenarios: Systematic exploration of uncertainties and the role of atmospheric chemistry". In: *Geophysical Research Letters* 39.9 (2012). DOI: https://doi.org/10.1029/2012GL051440. eprint: https://agupubs.onlinelibrary.wiley.com/doi/pdf/10.1029/2012GL051440. URL: https://agupubs.onlinelibrary.wiley.com/doi/abs/10.1029/2012GL051440.

[33] J. Peischl et al. "Quantifying Methane and Ethane Emissions to the Atmosphere From Central and Western U.S. Oil and Natural Gas Production Regions". In: *Journal of Geophysical Research: Atmospheres* 123.14 (2018), pp. 7725–7740. DOI: https://doi.org/10.1029/2018JD028622. eprint: https://agupubs.onlinelibrary.wiley.com/doi/pdf/10.1029/2018JD028622. URL: https://agupubs.onlinelibrary.wiley.com/doi/abs/10.1029/2018JD028622.

[34] O. Schneising et al. "Remote sensing of methane leakage from natural gas and petroleum systems revisited". In: *Atmospheric Chemistry and Physics* 20.15 (2020), pp. 9169–9182. DOI: 10.5194/acp-20-9169-2020. URL: https://acp.copernicus.org/articles/20/9169/2020/.

[35] Olaf Ronneberger, Philipp Fischer, and Thomas Brox. "U-Net: Convolutional Networks for Biomedical Image Segmentation". en. In: *Medical Image Computing and Computer-Assisted Intervention – MICCAI 2015*. Ed. by Nassir Navab et al. Lecture Notes in Computer Science. Cham: Springer International Publishing, 2015, pp. 234–241. ISBN: 978-3-319-24574-4. DOI: 10.1007/978-3-319-24574-4_28.

[36] Tom R. Andersson et al. "Seasonal Arctic sea ice forecasting with probabilistic deep learning". In: *Nature Communications* 12.1 (Aug. 2021), p. 5124. ISSN: 2041-1723. DOI: 10.1038/s41467-021-25257-4. URL: https://doi.org/10.1038/s41467-021-25257-4.

[37] Tai-Long He et al. "Deep Learning to Evaluate US NOx Emissions Using Surface Ozone Predictions". In: *Journal of Geophysical Research: Atmospheres* 127.4 (2022). e2021JD035597 2021JD035597, e2021JD035597. DOI: https://doi.org/10.1029/2021JD035597. eprint: https://agupubs.onlinelibrary.wiley.com/doi/pdf/10.1029/2021JD035597. URL: https://agupubs.onlinelibrary.wiley.com/doi/abs/10.1029/2021JD035597.

[38] T.-L. He et al. "Inverse modelling of Chinese $NO_x$ emissions using deep learning: integrating in situ observations with a satellite-based chemical reanalysis". In: *Atmospheric Chemistry and Physics* 22.21 (2022), pp. 14059–14074. DOI: 10.5194/acp-22-14059-2022. URL: https://acp.copernicus.org/articles/22/14059/2022/.

[39] Varvara E. Zemskova et al. "A deep-learning estimate of the decadal trends in the Southern Ocean carbon storage". In: *Nature Communications* 13.1 (July 2022), p. 4056. ISSN: 2041-1723. DOI: 10.1038/s41467-022-31560-5. URL: https://doi.org/10.1038/s41467-022-31560-5.

[40] Yann LeCun, Yoshua Bengio, and Geoffrey Hinton. "Deep learning". In: *Nature* 521.7553 (May 2015), pp. 436–444. ISSN: 1476-4687. DOI: 10.1038/nature14539. URL: https://doi.org/10.1038/nature14539.

[41] Saining Xie et al. *Aggregated Residual Transformations for Deep Neural Networks*. 2017. DOI: 10.1109/CVPR.2017.634.

[42] R.V. Kochanov et al. "HITRAN Application Programming Interface (HAPI): A comprehensive approach to working with spectroscopic data". In: *Journal of Quantitative Spectroscopy and Radiative Transfer* 177 (2016). XVIIIth Symposium on High Resolution Molecular Spectroscopy (HighRus-2015), Tomsk, Russia, pp. 15–30. ISSN: 0022-4073. DOI: https://doi.org/10.1016/j.jqsrt.2016.03.005. URL: https://www.sciencedirect.com/science/article/pii/S0022407315302466.

[43] Balaji Lakshminarayanan, Alexander Pritzel, and Charles Blundell. *Simple and Scalable Predictive Uncertainty Estimation using Deep Ensembles*. 2017. arXiv: 1612.01474 [stat.ML].